Nuclear Science and Techniques (2023) 34:181
https://doi.org/10.1007/s41365-023-01331-y

Enhancing betavoltaic nuclear battery performance with 3D P^+PNN^+ multi-groove structure via carrier evolution

Hou-Jun He[1,2,3] · Yun-Cheng Han[1] · Xiao-Yu Wang[1,4] · Yu-Min Liu[3] · Jia-Chen Zhang[1,2] · Lei Ren[1,2] · Ming-Jie Zheng[1]

Received: 4 May 2023 / Revised: 21 June 2023 / Accepted: 10 July 2023 / Published online: 30 November 2023

Abstract
Betavoltaic nuclear batteries offer a promising alternative energy source that harnesses the power of beta particles emitted by radioisotopes. To satisfy the power demands of microelectromechanical systems (MEMS), 3D structures have been proposed as a potential solution. Accordingly, this paper introduces a novel 3D ^{63}Ni–SiC-based P^+PNN^+ structure with a multi-groove design, avoiding the need for PN junctions on the inner surface, and thus reducing leakage current and power losses. Monte Carlo simulations were performed considering the fully coupled physical model to extend the electron–hole pair generation rate to a 3D structure, enabling the efficient design and development of betavoltaic batteries with complex 3D structures. As a result, the proposed model produces the significantly higher maximum output power density of 19.74 μW/cm^2 and corresponding short-circuit current, open-circuit voltage, and conversion efficiency of 8.57 μA/cm^2, 2.45 V, and 4.58%, respectively, compared with conventional planar batteries. From analysis of the carrier transport and collection characteristics using the COMSOL Multiphysics code, we provide deep insights regarding power increase, and elucidate the discrepancies between the ideal and simulated performances of betavoltaic batteries. Our work offers a promising approach for the design and optimization of high-output betavoltaic nuclear batteries with a unique 3D design, and serves as a valuable reference for future device fabrication.

Keywords Betavoltaic nuclear battery · High-output power density · Three-dimensional structure · Carrier drift–diffusion · Carrier recombination · Carrier collection efficiency

1 Introduction

With remarkable performance, compact size, and high-volume production, microelectromechanical systems (MEMS) have attracted tremendous interest for various applications ranging from mobile electronics to deep-sea surveys, implantable medical devices, and autonomous wireless sensor networks. However, the development of micro-batteries capable of outputting power of 1–100 μW, long service life, and fitting within the size range of 1 μm–10 mm has become a critical challenge for MEMS applications [1–3]. Recently, betavoltaic nuclear batteries have emerged as a highly attractive energy option for MEMS applications, with the potential advantages of long operational life, high energy density, ultra-miniature size, and strong anti-interference [4–7].

The performance of betavoltaic nuclear batteries is governed by radioisotope source characteristics, device geometry, and semiconductor converter properties. The corresponding relationship can be mathematically expressed as:

$$P_{\mathrm{m}} = AE_{\mathrm{avg}}\eta_{\mathrm{s}}(1-r)\eta_{\mathrm{c}} = AE_{\mathrm{avg}}\eta_{\mathrm{s}}(1-r)\frac{QV_{\mathrm{OC}}FF}{\varepsilon}, \quad (1)$$

where A is radioisotope activity determined by the radioisotope half-life, E_{avg} is the average β-decay energy dictating the total input power driving the converter, η_{s} is the fraction of β-energy emitted to the total decay energy of the radioisotope source, r is the reflectivity coefficient, η_{c} is the

This work was supported by Anhui Provincial Key R&D Program (No. 202104g0102007), Jiangxi Provincial Department of Education Science and Technology Research Youth Project (GJJ200763), Hubei Provincial Natural Science Foundation of China (No. 2022CFB575), Hefei Municipal Natural Science Foundation (No. 2022011); Ministry of Education Industry-Education Cooperation Project (No. 202102647014), Science Island Graduate Innovation and Entrepreneurship Fund Project (No. KY-2022-SC-04).

Extended author information available on the last page of the article

energy conversion efficiency of the semiconductor converter, Q is the carrier collection efficiency, V_{OC} is the open-circuit voltage, FF is the fill factor, and ε is the effective ionization energy to generate an electron–hole pair (EHP). The overall conversion efficiency can be expressed as: $\eta_{tot}=\eta_s(1-r)\eta_c$. The output power of betavoltaic nuclear batteries depends on significant losses, such as self-absorption loss $(1-\eta_s)$ in the radioisotope source, backscattering loss (r) at the semiconductor interface, and carrier collection loss $(1-Q)$ outside the depletion region [8–10]. To maximize the energy coupling between the radioisotope and semiconductor, it is crucial to increase their face-to-face area while reducing self-absorption and backscattering effects. Additionally, η_c depends on the material properties of the semiconductor, including bandgap, depletion region width, and carrier diffusion length. Q, V_{OC}, and FF can be improved via optimization of doping concentrations and junction width to increase the depletion region width and carrier diffusion length, ensuring that the β-particle penetration depth matches the converter scale length.

As the conventional planar configuration of betavoltaic nuclear batteries uses only one side of the radioisotope source attached to the semiconductor converter, the output power and conversion efficiency are limited. A high activity (A) or input power (P_{in}) requires a thick source layer, but this results in stronger self-absorption effects and smaller η_s, saturating $A\cdot\eta_s$. The directional loss is approximately 50%, and the backscattered loss significantly reduces the device efficiency by up to 25% [10, 11]. Although efforts have been made to improve the conversion efficiency and output power of betavoltaic nuclear batteries, including use of a reflector to reduce directional loss and backscattered loss [12], optimization of the junction depth and doping concentration to increase the carrier collection efficiency [13–16], use of an extra graded N layer to reduce radiation-induced EHPs recombination loss [17], and adoption of radioisotope sources with higher particle energy to increase input power [18]; their reported values remain limited by the effective loading activity of the radioisotope source as well as the coupling efficiency between the source and device, i.e., the limitation of $A\eta_s(1-r)$. As a result, the respective output power is only 0.1–50 nW for practical and tested batteries [18–22] and 10–400 nW for theoretically predicted ones [13–15, 19, 23, 24], falling short of meeting the power requirements of MEMS [25].

To achieve higher performance in betavoltaic nuclear batteries, $A\eta_s(1\text{-}r)$ can be increased over a wide range using specific types of radioisotope sources and semiconductor materials. Increasing the specific surface area of the converter can enable a higher loading amount of radioisotope sources, leading to larger $A\eta_s(1-r)$ and higher output power. Compared with two-dimensional (2D) planar structures, three-dimensional (3D) structures with a larger specific surface area can significantly increase the output power density owing to three factors: (i) more radioisotope sources can fill the interspace of 3D structures, (ii) the thinning of radioisotope sources in 3D structures significantly reduces the self-absorption effects, and (iii) the combination of a radioisotope source with 3D structures leads to the interaction of beta particles with the converter in all directions, increasing the collection efficiency of the beta particles.

In recent years, the use of 3D structures in betavoltaic nuclear batteries has demonstrated significant potential for improving the corresponding specific surface area and conversion efficiency; thus, they are promising options for meeting MEMS power demands [26–29]. However, conventional 3D structures require preparation of PN or PIN junctions on the inner surface of the microstructure, which significantly affects the leakage current and output performance [28]. This is a predominant reason why the device performance is far from ideal, even up to several orders of magnitude, so full use of the 3D structure is challenging. Moreover, while Monte Carlo simulations [15, 30] and empirical formulas [31, 32] are widely employed to calculate the distribution of the EHP generation rate [$G(x)$] in betavoltaic nuclear batteries with 2D diode structures, the EHP generation rate is rarely evaluated in 3D structured converters combined with radioisotope sources distributed in 3D space. Most currently available models for $G(x)$ in 3D structured converters only describe specific structures with fixed source and device geometries, and cannot accurately evaluate the EHP distribution in 3D structures, highlighting the need for a precise model to advance the development of 3D batteries.

This paper introduces a novel approach that addresses these issues, utilizing a ^{63}Ni-SiC-based (P^+PNN^+) structure with a multi-groove design, enabling the epitaxial growth of graded P and N layers on the substrate without the need of preparing PN junctions on the inner surface of the microstructure. This approach has the potential to significantly reduce leakage current and power losses, thereby narrowing the gap between theoretical predictions and experimental results. In addition, a novel formulaic model is proposed for calculating the complex EHP generation rate in 3D-structured betavoltaic nuclear batteries. The model considers the intricate 3D structure of the converter and radioisotope source, enabling accurate evaluation of the EHP distribution in all possible 3D structures resulting from changes in their geometries. Our fully coupled model, combined with the COMSOL Multiphysics code, involves the entire physical process of carrier evolution, including β-particle generation, energy deposition, radiation-carrier generation, drift–diffusion, and recombination. This study provides valuable insight into the internal mechanisms of carrier transport, collection characteristics, and power increase. From the results, our approach demonstrates maximized output power density with optimized source thickness, converter geometry, doping

concentration, and width of each region, outperforming conventional planar batteries. Our novel $G(x)$ model provides a critical tool for designing and optimizing 3D structured betavoltaic nuclear batteries, with potential applications in other betavoltaic nuclear batteries.

2 Model and method

2.1 Device structure

Figure 1a depicts a ^{63}Ni–SiC-based betavoltaic nuclear battery with a multi-groove structure, characterized by the ridge width [d], ridge spacing [t], and groove depth [H_source]. The converter comprises four layers: a P^+-SiC layer, graded P-SiC layer, graded N-SiC layer, and N^+-SiC layer, with thicknesses of H_P^+, H_P, H_N, H_N^+ (the N^+-layer thickness is slightly larger than that of H_N^+), respectively. The ^{63}Ni source was filled in multi-grooves, surrounded by converters at the sides and bottom (front and rear sides not shown), and enclosed by a metal electrode at the top. This design reduces the directional and electrode shielding losses compared with conventional planar diode structures. The rectangular top section of the device has the area of 1 cm × 1 cm. To prevent PN junction shorting and metal–semiconductor contact formation, techniques such as nitride passivation, plasma-enhanced chemical vapor deposition, and atomic layer deposition can be employed to grow a thin insulating layer (e.g., Si_3N_4, SiO_2, and Al_2O_3) with a thickness of 10–100 nm [33–36]. This layer effectively blocks the flow of electrons or holes, achieving insulation between the source and semiconductor devices, while having a negligible impact on the energy deposition of the source decay energy in the device.

To ensure good Ohmic contact, the doping concentrations of heavily doped P^+-SiC and N^+-SiC layers are 10^{19} and 10^{18} cm^{-3}, respectively. The P- and N-SiC layers serve as the core regions of the betavoltaic nuclear battery, generating an internal electric field [$\rightarrow_{E_I}$] to separate the radiation-induced EHPs. These layers are lightly doped to obtain larger depletion region width [W_d] and minority diffusion length [L_n or L_p], and promote EHP collection, as depicted in Fig. 1b. The gradient interface between the P^+/P and N/N^+ layers generate an extra electric field [$\rightarrow_{E_P}$ and $\rightarrow_{E_N}$], which reduces battery surface recombination and enhances EHP collection. In this 3D structure, EHPs are mainly generated in the ridges, and hence these areas contribute the most to the output power. Monte Carlo simulations and COMSOL Multiphysics were used to optimize the structural parameters, including the thickness of each doping region, doping concentration, ridge width, and ridge spacing, and predict the battery output performance.

^{63}Ni source was selected as the beta source due to its long half-life (approximately 100 years), moderate decay energy (E_{avg} = 17.4 keV, E_{max} = 66.9 keV), and solid metal form, which allows easier and safer handling. SiC was selected as the converter semiconductor material because of its desirable properties including low leakage current density, higher radiation damage threshold, higher conversion efficiency, and excellent tolerance to harsh environments, i.e., extreme temperatures, wear, chemical exposure, and radiation [37–39]. Moreover, the development of SiC etching

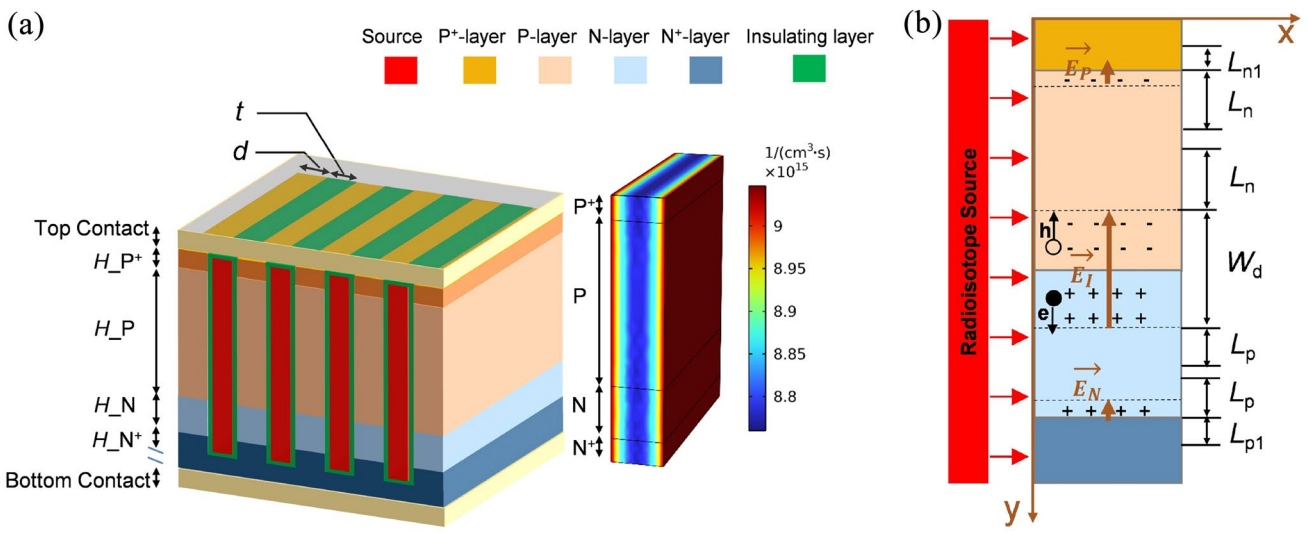

Fig. 1 (Color online) **a** Schematic 3D diagram showing part of the proposed battery and the distribution of the electron–hole pair (EHP) generation rate in the innermost ridge with t = 0.8 μm and d = 1.2 μm; **b** Structure principal diagram of SiC P^+PNN^+ betavoltaic nuclear battery. Dimensions are not in scale

technology has enabled the fabrication of microgroove structures with high aspect ratio [39].

2.2 Methods

2.2.1 Radiation-induced carrier generation in 3D diode structures

2.2.1.1 Model for radiation-induced carrier generation rate in 3D diode structures The distribution of the EHP generation rate in a betavoltaic nuclear battery is governed by the energy deposition of beta particles in the converter, which significantly affects the output performance. In the conventional planar diode structure depicted in Fig. 2b, the energy deposition [$E_{dep}(x)$] along the radiation transport depth [x] in bulk SiC was calculated via a Monte Carlo simulation with the Geant4 radiation transport toolkit, using a rectangular ^{63}Ni source with a full energy spectrum. The ^{63}Ni source is characterized by the specific activity of 5.68 Ci/g, 100% abundance, and density of 8.9 g/cm^3, with isotropic emission of beta particles. SiC has the bandgap width of 3.26 eV, relative dielectric constant of 9.7, density of 3.21 g/cm^3, and intrinsic carrier concentration of 7.4×10^{-9} cm^{-3}, derived using the widely employed formula [40]. $G(x)$ is obtained and expressed as:

$$G(x) = \frac{A \cdot E_{dep}(x)}{\varepsilon} = G_0 \exp(-\alpha x), \tag{2}$$

where A is the activity of the radioisotope, ε is the average energy needed to generate an EHP, commonly considered as 6.88 eV for SiC [41], and G_0 and α are the surface EHP generation rate and absorption coefficient, respectively. $G(x)$ of ^{63}Ni sources with varying thickness [t] is presented in Fig. 2c, and the corresponding G_0 and α are derived by fitting $G(x)$. The dependences of G_0 and α on the source thickness [t] are then fitted, as demonstrated in Fig. 2d. Consequently, $G(x)$ considering different source thicknesses is expressed as: $G(x,t) = A_1(1-e^{-\mu_1 t})e^{-(A_2 e^{-\mu_2 t}+B_2)x}$, the fitting parameters for which are provided in Table 1. Figure 2c shows that the saturation thickness of the ^{63}Ni source is 3 μm, consistent with previous work [24, 42]. The penetration depth of

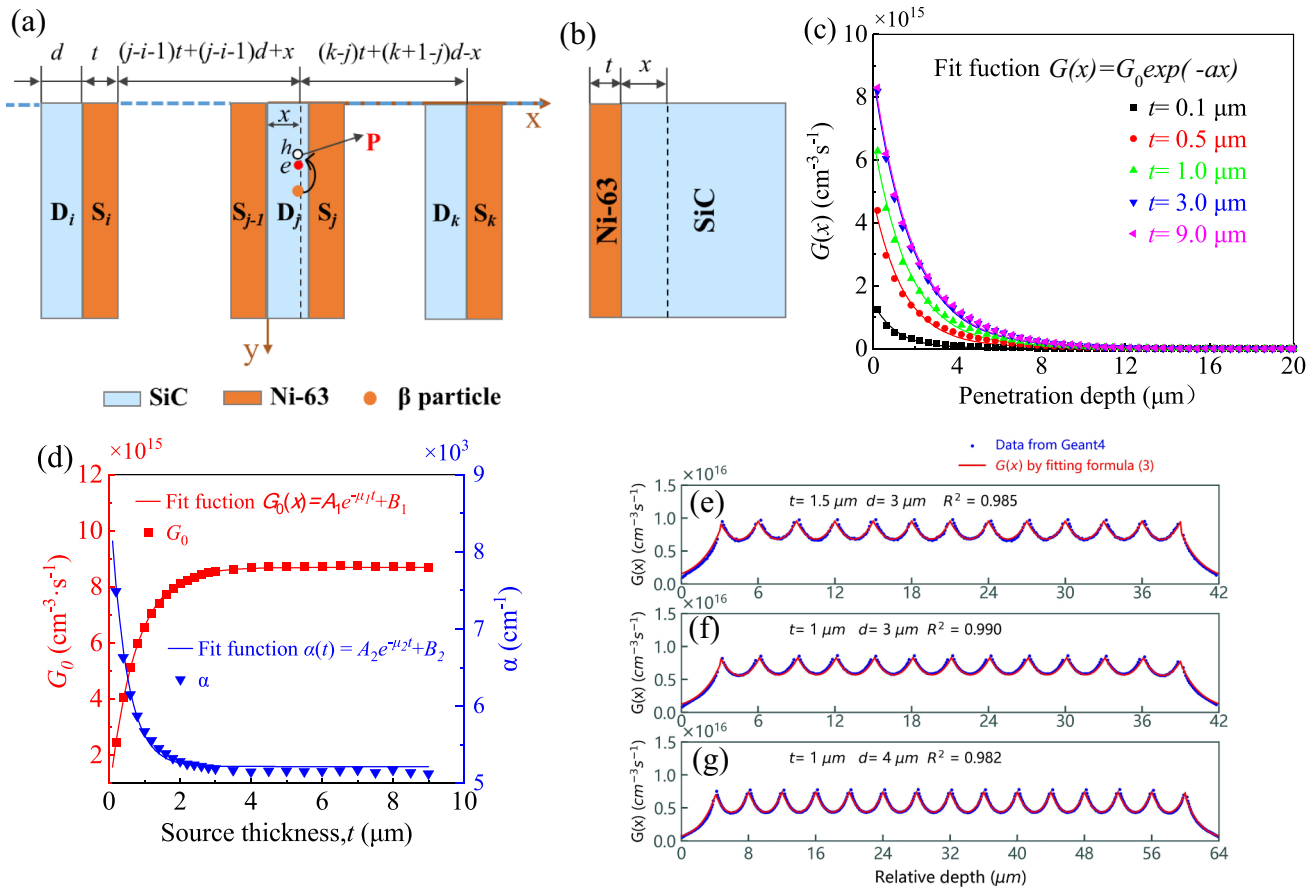

Fig. 2 (Color online) Schematics of **a** 3D and **b** 2D converters; **c** EHP generation rates along penetration depth and **d** surface EHP generation rate and absorption coefficient for different source thicknesses in 2D converters; EHP generation rates in 3D converter with **e** 1.5 μm ridge spacing and 3 μm ridge width, **f** 1 μm ridge spacing and 3 μm ridge width, **g** 1 μm ridge spacing and 4 μm ridge width

β particles emitted from ^{63}Ni is 10.2 μm in SiC, defined as the location where 99% of the total energy deposition occurs according to Alam [8].

To accurately model the energy deposition and EHP generation rate in a multi-groove betavoltaic nuclear battery, it is essential to consider the superposition contributions of all the isotope sources and ridges. This involves extending $G(x,t)$ of the 2D structure to that of the 3D structure. Figure 2a characterizes the penetration distance distribution of β particles released by ^{63}Ni isotope sources, where D_j denotes the jth layer converter (the jth ridge of the proposed battery) and S_j indicates the jth ^{63}Ni layer. At a random location of the EHPs generated in converter D_j (specified by reference site P), the distance between P and source S_{j-1} is represented by $[x]$. Converter D_j is exposed to $[j-1]$ layers of isotope sources on its left, and the β particles emitted from the ith ($i<j$) source must traverse a total source thickness of $[(j-i-1)t]$ and a total converter thickness of $[(j-i-1)d+x]$ to reach reference site P. Similarly, D_j is exposed to $[n+1-j]$ layers of sources on its right, and the β particles emitted from the kth ($j \le k \le n$) source must penetrate a total source thickness of $[(k-j)t]$ and a total converter thickness of $[(k+1-j)d-x]$ to reach P. During this process, the energy of the beta particles decays exponentially with penetration distance, and the EHP generation rate of D_j is given by:

$$G_j(x,t) = \sum_{i=1}^{i=j-1} \left\{ G_0(t) e^{-\alpha(t)((j-i-1)d+x)} e^{-\gamma(t)(j-i-1)t} \right\} + \sum_{k=j}^{k=n} \left\{ G_0(t) e^{-\alpha(t)((k+1-j)d-x)} e^{-\gamma(t)(k-j)t} \right\}, \quad (3)$$

where n is the layers of sources, $G_0(t)$ is the surface EHP generation rate, $\alpha(t)$ is the absorption coefficient of β-electron flux in SiC, and $\gamma(t)$ is the absorption coefficient of β-electron flux in ^{63}Ni, which are acquired via the equation in Table 1 based on Monte Carlo code simulation. The EHP generation rate of the $(n+1)$th converter can be expressed as $G_{n+1}(x,t) = G_1(d-x,t)$, owing to the symmetry of the multi-groove structure. Table 1 shows that the R^2 (R-squared or coefficient of determination) values are greater than 0.99, indicating the excellent fitting performance of the model.

2.2.1.2 Validation of electron–hole pair (EHP) generation rate model in 3D diode structures

Accurate prediction of the rate of EHP generation is essential for optimizing the design of 3D SiC-based betavoltaic nuclear batteries. Therefore, the validity and ability of the model to predict data from 3D multi-groove structures was demonstrated through comparison with original Geant4 data [$AE_{dep}(x)/\varepsilon$]. Figure 2e–g exhibit the reliability of the proposed EHP generation rate model, expressed by formula (3), with highly consistent $G(x,t)$ curves compared with the original Geant4 data for both ridge spacings of 1.5 and 1 μm, and ridge widths of 3 and 4 μm. The high R^2 values of 0.985, 0.990, and 0.982 for these curves indicate the accuracy of the model in calculating the EHP generation rates in 3D structures, rendering it a valuable tool for optimizing SiC-based betavoltaic nuclear batteries for high performance.

In the 2D converter, the EHP generation rate decreased exponentially with depth; whereas, the multi-groove 3D structure exhibits a unique distribution of higher EHP generation rates in the inner ridges and lower rates in the outermost ridges. The innermost ridges exhibit high EHP generation rates on the lateral surfaces, low rates in the middle, and a symmetrical distribution, matching the 3D EHP distribution in the inner ridge shown in Fig. 1a. These findings suggest that the proposed multi-groove 3D structure has the potential to significantly enhance the power output compared with the traditional 2D structure, particularly as the relative depth increases.

2.2.2 Model for radiation-induced current in 3D diode structures

Figure 1b illustrates that radiation-induced EHPs generated within the depletion region can be collected with 100% efficiency, whereas those generated outside the depletion region can only be collected after diffusion to the PN junction boundary, the P^+/P interface, or the N/N^+ interface. The $CE(y)$ was calculated using the equation [43]:

$$CE(y) = 1 - \tanh \frac{d(y)}{L}, \quad (4)$$

where $d(y)$ represents the distance from the depletion region boundary or the interfaces and is set to zero inside the depletion region. The electron and hole minority carrier diffusion

Table 1 Exponential fitting parameters and R-squared values for $G_0(t)$, $\alpha(t)$, and $\gamma(t)$

Equations	Fitting values	R^2
$G_0(t) = A_1 e^{-\mu_1 t} + B_1$	$A_1 = -8.14 \times 10^{15}$ cm^{-3}·s^{-1}, $\mu_1 = 1.35$ μm^{-1}, $B_1 = 8.69 \times 10^{15}$ cm^{-3}·s^{-1}	0.999
$\alpha(t) = A_2 e^{-\mu_2 t} + B_2$	$A_2 = 3638.76$ cm^{-1}, $\mu_2 = 2.19$ μm^{-1}, $B_2 = 5216.14$ cm^{-1}	0.992
$\gamma(t) = A_3 e^{-\mu_3 t} + B_3$	$A_3 = 8472.34$ cm^{-1}, $\mu_3 = 2.06$ μm^{-1}, $B_3 = 15344.09$ cm^{-1}	0.997

lengths L are expressed as L_{n1}, L_n, L_p, and L_{p1} in regions P^+, P, N, and N^+, respectively. The radiation-induced current density J_R can be expressed as:

$$J_R = \left(\sum_{i=1}^{i=n+1} q \int_0^{H_1} G_j(x,t)\mathrm{d}x \int_0^{H\_source} CE(y)\mathrm{d}y \int_0^{H_2} \mathrm{d}z \right) \Big/ S, \quad (5)$$

where q is the electron charge; H_1 is the ridge width [d]; and H_2 and S are the rectangular side length (1 cm) and area of the device (1 cm^2), respectively.

According to the drift–diffusion theory, nonequilibrium carriers generated within the depletion region and the neutral region outside the depletion region boundary within a minority diffusion length can be collected, thus contributing to the current density (J_R). The effective charge collection region (ECR) length, represented by $H\_ECR = (W_d + L_{n1} + 2L_n + 2L_p + L_{p1})$, determines J_R and can be maximized by increasing W_d, L_{n1}, L_n, L_p, and L_{p1}. Lower doping concentrations increase W_d and L, leading to higher EHP collection, as demonstrated in Fig. 3a, b, where W_d decreases from 7.58 µm to 30 nm and L_n decreases rapidly from 77.34 to 11.06 µm with increasing doping concentration from 10^{14} to 10^{19} cm^{-3}. L_p decreases more gradually over the same doping range. The minimum doping concentration in the P- and N-regions was 10^{14} cm^{-3} due to our facility's capacity to process low doping in SiC materials; whereas, the minimum doping concentration of the heavily doped P^+- and N^+-regions required $N_A = 10^{19}$ cm^{-3} and $N_D = 10^{18}$ cm^{-3}, respectively, to reduce the ohmic contact. To maximize H_ECR and J_R, the maximum values of W_d, L_{n1}, L_n, L_p, and L_{p1} should be adopted, as listed in Table 2 and detailed in Supplementary Materials S1 and S2.

2.2.3 Battery output characteristic model and simulation

The electron (hole) concentration [n (p)] inside the semiconductor converter device is governed by the carrier continuity equation as follows:

$$\frac{\partial n}{\partial t} = \frac{1}{q}\nabla \cdot j_n + G - R_n, \quad (6)$$

$$\frac{\partial p}{\partial t} = -\frac{1}{q}\nabla \cdot j_p + G - R_p, \quad (7)$$

where j_n (j_p) is the electron (hole) current density, G is the EHP generation rate derived from Eq. (3), and R_n (R_p) is the electron (hole) recombination rate. j_n (j_p) can be described by the drift and diffusion processes [44] as:

$$j_n = nq\mu_n E + qD_n \nabla n, \quad (8)$$

$$j_p = pq\mu_p E - qD_p \nabla p, \quad (9)$$

where E is the sum of the external and internal electric fields generated by the diffusion of EHPs. These relationships are governed by the Poisson equation:

$$\frac{\partial E}{\partial x} = \frac{q\left(N_D - N_A + p - n\right)}{\epsilon_0 \epsilon_r}, \quad (10)$$

Table 2 Maximum depletion region and minority carrier diffusion length in each region of the converter

W_{d_max} (µm)	L_{n1_max} (µm)	L_{n_max} (µm)	L_{p_max} (µm)	L_{p1_max} (µm)
7.58	11.06	77.34	11.44	6.15

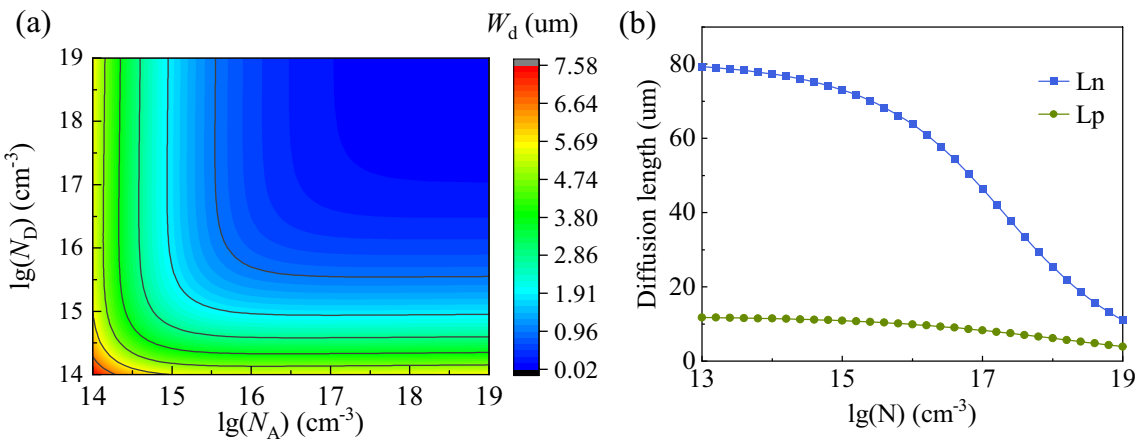

Fig. 3 **a** Depletion region width and **b** minority diffusion length with doping concentration

where ρ is the charge density, ϵ_0 is the vacuum permittivity, ϵ_r is the relative permittivity of the semiconductor, and N_D (N_A) is the concentration of donor (acceptor).

2.2.3.1 Current–voltage characteristics of ideal PN junction diodes The current–voltage (J–V) characteristics of an ideal long PN junction diode can be derived assuming that the external voltage drops entirely in the depletion region, the diode operates under a low injection level (i.e., the excess carrier concentration is much smaller than the equilibrium majority carrier concentration), there is no recombination or generation current in the space-charge region, the semiconductor is nondegenerate, and the length of the P- (N-) region is much larger than the diffusion length[45, 46].

Under these assumptions, the J–V relationship of the neutral areas ($E=0$) of the P- and N-regions can be obtained by solving the continuity Eqs. (6–7) and current Eqs. (8–9). Ignoring the recombination and generation currents in the space-charge region, the J–V characteristics of an ideal diode are given by:

$$J = J_{SC} - \left(J_P + J_N\right) = J_{SC} - J_0\left[\exp\left(\frac{eV}{kT}\right) - 1\right], \tag{11}$$

where J_{SC} is the short current, equals to radiation-induced current J_R; k is Boltzmann's constant; T is the absolute temperature (300 K in this work); V is the bias voltage; and J_0 is the leakage current density of the PN junction.

The open-circuit voltage is derived as $J=0$ A.

$$V_{OC} = \frac{kT}{q}\ln\left(\frac{J_{SC}}{J_0} + 1\right) \tag{12}$$

Then, the maximum output power P_m can be described as:

$$P_m = J_{SC}V_{OC}FF, \tag{13}$$

where FF is the fill factor, which can be derived using the open-circuit voltage [13]. J_0 is determined by the diffusion efficiency and diffusion length of the minority carriers, and the doping concentrations, shown in S3 of the Supplementary Materials. Using this ideal diode model, the battery performance can be predicted quickly, and the optimal battery structure can be determined based on the J–V characteristic numerical model.

2.2.3.2 Current–voltage characteristics calculation using COMSOL Multiphysics The J-V characteristics of real diodes differ from those of ideal diodes owing to the various assumptions made for ideal PN junction diodes. Therefore, an accurate method is essential to simulate the J–V characteristics of real diodes, considering the generation, recombination, and drift of charge carriers, as well as the real characteristics of the semiconductor material.

COMSOL Multiphysics is a powerful tool for simulating the current–voltage characteristics of realistic situations by solving partial differential equations that incorporate real physical phenomena. The simulation utilizes various physical models, including the Monte Carlo simulation for calculating the EHP generation rate in 3D diode structures (Eq. 3), the Shockley–Read–Hall model for trap-assisted recombination (Eq. 14) [45], and the low-field mobility model for determining the minority carrier mobility (Eqs. S4–S5 in the Supplementary Materials). Additionally, the carrier lifetime model is described in Eqs. S6–S7 in the Supplementary Materials.

$$\begin{aligned} R &= \frac{C_p C_n N_t\left(np - n_i^2\right)}{C_n\left(n + n_i\exp\left(\frac{E_t - E_i}{kT}\right)\right) + C_p\left(p + n_i\exp\left(\frac{E_i - E_t}{kT}\right)\right)} \\ &= \frac{np - n_i^2}{\tau_p\left(n + n_i\exp\left(\frac{E_t - E_i}{kT}\right)\right) + \tau_n\left(p + n_i\exp\left(\frac{E_i - E_t}{kT}\right)\right)} \end{aligned} \tag{14}$$

here C_n (C_p) is the electron (hole) capture coefficient, n_i is the intrinsic carrier concentration, τ_n (τ_p) is the electron (hole) minority lifetime given by Eqs. S6–S7 of the Supplementary Material, E_t is the recombination center (defect) level, and E_i is the intrinsic Fermi level. The defect energy level is set as $E_t = E_i$, and the defect density is $N_t = \frac{1}{C_n\tau_n} = \frac{1}{C_p\tau_p}$.

Solving partial differential Eqs. (6–10), we obtained important information on the electric field, carrier recombination, and electron (hole) current density, enabling prediction of crucial electrical parameters, including the short-circuit current [J_{SC}], open-circuit voltage [V_{OC}], and output power [P_m]. Ultimately, with this approach, the behavior of diodes can be accurately modeled, which is vital for optimizing their performance and ensuring that they meet the requirements of various real-world applications.

3 Results and discussion

3.1 Performance calculated using ideal diode model

To optimize the structure of the proposed battery and maximize its output power density, a parametric sweep was conducted in the numerical model to adjust variables including the single-source thickness (ridge spacing, t); single-converter thickness (ridge width, d); thicknesses of the P^+-, P-, N-, and N^+-regions (H_P^+, $H_$P, $H_$N, and H_N^+); acceptor concentration of P-region (N_a); and donor concentration of N-region (N_d). Possible values of t and d are in the range of 0.1–10 μm with a 0.1 μm step size for each. It is worth noting that the source thickness is fixed

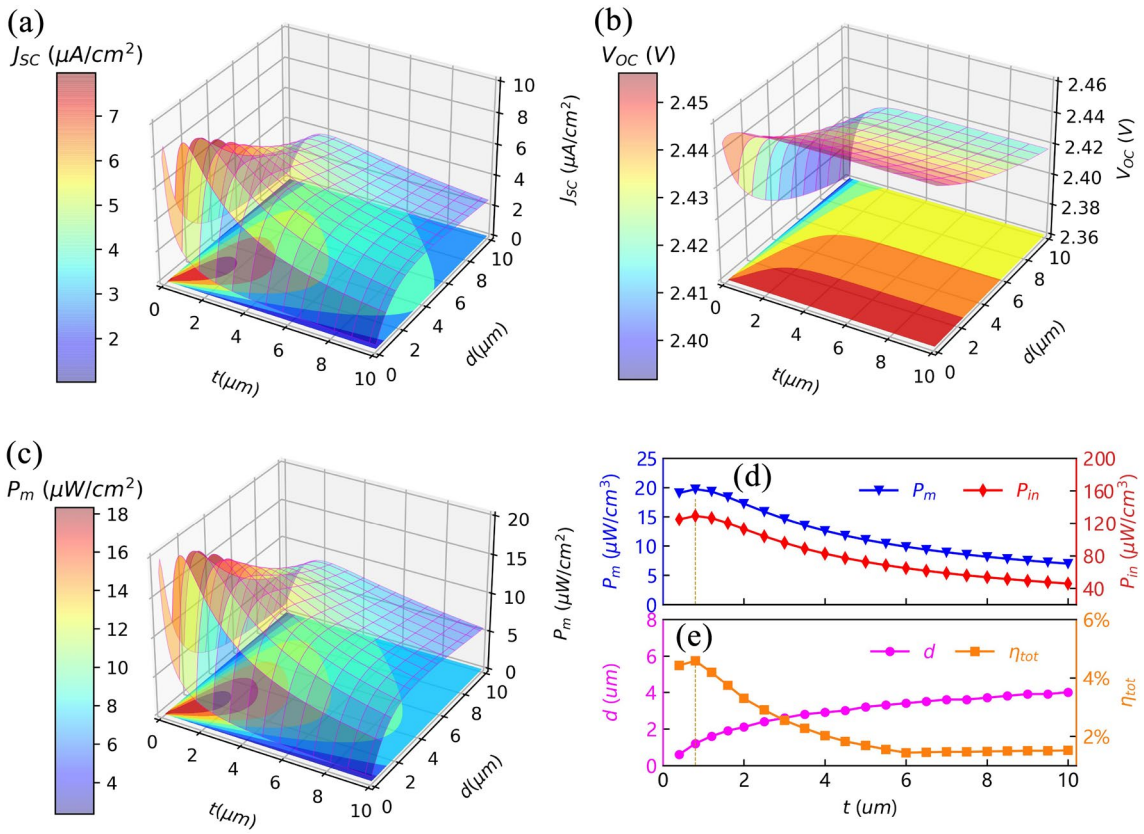

Fig. 4 (Color online) Effects of the ridge spacing [t] and ridge width [d] on the **a** J_{SC}, **b** V_{OC}, **c** P_m; the dependences of **d** P_m, P_{in}, **e** d, and η_{tot} on t. N_a and N_d are both set to 1×10^{14} cm^{-3}; H_P and H_N are set to 158 μm and 26 μm, respectively, approximately equal to $(2L_{n\_max}+W_{d\_max}/2)$ and $(2L_{p\_max}+W_{d\_max}/2)$

to the saturation thickness of 3 μm as t is greater than 6 μm, and evenly distributed on the inner surface of the microgroove. The feasible ranges for H_P and H_N are 1–250 μm and 1–60 μm, respectively, while N_a and N_d can range from 1×10^{14} to 7.94×10^{18} cm^{-3} and 1×10^{14} to 7.94×10^{17} cm^{-3}, respectively. The values for H_P^+ and H_N^+ correspond to 10 and 6 μm, which are close to the minority carrier diffusion length in the P^+-region and N^+-region. Additionally, the heavily doped P^+-region and N^+-region are assigned acceptor concentration and donor concentration values of 1×10^{19} and 1×10^{18} cm^{-3}, respectively.

3.1.1 Optimizing ridge spacing and width

The output power of a betavoltaic nuclear battery depends on the amount of beta particle energy deposited in the converters and the efficient collection of radiation-induced EHPs. The coupling between the radiation source and the device is crucial for enhancing the output power. To illustrate the impacts of t and d on the output performance of the betavoltaic battery, the 3D surface contours of the short-circuit current density (J_{SC}), open-circuit voltage (V_{OC}), and maximum output power density (P_m) were plotted, as shown in Fig. 4.

As depicted in the 3D surface wireframe perpendicular to the d direction in Fig. 4a, J_{SC} initially increases rapidly, but subsequently decreases as t increases, reaching a peak value with t of 0.1–2.2 μm. Additionally, the dependence of J_{SC} on d exhibits a similar trend, reaching its peak with d of 0.2–4.0 μm. The bottom-projected contour shows that the optimal values of J_{SC} are achieved when d is in the range of 0.2–3 μm and t ranges from 0.1 to 2 μm. The maximum J_{SC} of 8.57 μA/cm^2 is achieved by combining $t=0.8$ μm and $d=1.2$ μm.

Figure 4b demonstrates that V_{OC} initially increases as t increases and reaches saturation at $t=2$ μm, while it decreases with an increase in d. Nevertheless, overall, V_{OC} is not highly sensitive to variations in t and d, with a range of 2.36–2.46 V. Due to the minor variation in V_{OC}, P_m is primarily determined by J_{SC}. The relationship between P_m and variations in t and d exhibit similar trend to that of J_{SC}, with a rapid initial increase and a subsequent slow decrease with increasing t or d, as illustrated in Fig. 4c. The

maximum P_m value of 19.73 μW/cm^2 is attained at $t = 0.8$ μm and $d = 1.2$ μm.

The factors affecting the output power mainly include A, η_s, $(1-r)$, Q, V_{OC}, and FF. With varying t and d, A, η_s, $(1-r)$, V_{OC}, and FF exhibit relative increases of 9844.28%, 578.19%, 1956.94%, 4.14% and 0.21%, respectively, while Q remains unchanged at 45.64%. Therefore, the key factor affecting the output power is the coupling of A, η_s, and r. For the detailed calculation process, please refer to Supplementary Material S4.

The input power [P_{in}] can be calculated by combining A, η_s, and r, as $P_{in} = AE_{avg}\eta_s(1-r)$. Figure 4d–e present the maximum output power [P_m] and its corresponding optimized ridge width [d] of 0.2–4.0 μm, for different source thicknesses [t]. We found that P_m is determined by the coupling of A, η_s and r, i.e., P_{in}. The optimized value of d gradually saturates with increasing t, consistent with the phenomenon of energy deposition saturation in the converter with increasing d. Additionally, the overall conversion efficiency [η_{tot}] increases and then decreases with t, reaching a saturated value of approximately 1.5%, and η_{tot} corresponding to maximum P_{in} and P_m is 4.58%.

In the proposed battery, smaller ridge spacing and ridge width can improve the source activity and reduce the self-absorption effect. However, excessively thin converters may result in a lower $(1-r)$ and do not match the particle penetration depth, leading to a reduced P_{in}. Therefore, a tradeoff between t and d is necessary to maximize the power density.

3.1.2 Optimizing widths of P-region and N-region

After optimizing t and d, we investigated the dependence of J_{SC}, V_{OC}, and P_m on the widths of the P- and N-regions for betavoltaic nuclear batteries, as shown in Fig. 4a–c. Increasing H_P results in an initial increase and subsequent saturation of J_{SC}, V_{OC}, and P_m. This trend can be attributed to the increase in the radioisotope source activity with H_P, which generates more EHPs in the ECR. However, when H_P exceeds the ECR length, the performance metrics reach saturation. Specifically, J_{SC}, V_{OC}, and P_m saturate when H_P reaches 160 μm, and an additional increase of 10 μm results in a negligible increase of less than 1%. Similarly, J_{SC}, V_{OC}, and P_m present a similar trend with H_N, showing a gradual rise and saturation at $H\_N = 24$ μm. This phenomenon can be attributed to the longer minority carrier diffusion length ($L_n = 77.34$ μm) of the P-region compared with that of the N-region ($L_p = 11.44$ μm), and their saturation values of H_P and H_N are around twice L_n and L_p, respectively. Therefore, $H_$source should not exceed 200 μm, where H_P^+ and H_N^+ are 6 and 10 μm, respectively, and H_P and H_N should not exceed their saturation values, corresponding to 160 and 24 μm.

Figure 5d shows that A linearly increases with H_P from 0.51 to 6.59 Ci (by 1204.00%), while Q first increases and then decreases with the relative change rate of 164.92%. The optimization of H_P reveals that factor A is the dominant factor affecting the output power, and factor Q is secondary. Although A and Q show different trends with changes in H_P, their products, $A{\cdot}Q$ and P_m, exhibit consistent trends, further confirming that A and Q are the key factors affecting P_m, as shown in Fig. 5e. However, V_{OC} and FF increase minimally by 1.81% and 0.09%, while η_s and $(1-r)$ remain unchanged at 61.53% and 48.77%, respectively. Please refer to Supplementary Material S4 for detailed calculations.

As depicted in Fig. 5f, for the structure with $H_$source = 200 μm, J_{SC} and P_m initially increase with H_P and then decline instead of continuously increasing. This behavior is due to the contribution of H_N to J_{SC}, and P_m outweighs that of H_P when H_P approaches its saturation thickness. Therefore, when optimizing the widths of the P- and N-regions, the balance between H_P and H_N should be considered, as the combination of $H\_P = 156$ μm and $H\_N = 28$ μm achieves the maximum P_m of 19.74 μW/cm^2. A longer P-region is more suitable for a betavoltaic nuclear battery with a P^+PNN^+ junction structure because it is more conducive to enhancing the collection of EHPs owing to the larger minority carrier lifetime and mobility compared with the N-region, as shown in Fig. S2 in the Supplementary Material.

3.1.3 Optimizing doping concentration in P- and N-regions

Based on the analysis in Sect. 2.2.2, the doping concentration plays a crucial role in determining the depletion width and minority carrier diffusion length of the betavoltaic nuclear battery, which significantly affects the collection efficiency of the EHPs and the output performance of the battery.

Figures 5c and 6a illustrate the effects of N_a and N_d on J_{SC}, V_{OC}, and P_m for the proposed battery. As shown in Fig. 6a, J_{SC} increases with a decrease in N_a owing to its beneficial effect of expanding the minority carrier diffusion length and depletion region width to promote EHP collection, as depicted in Fig. 3. The variation in J_{SC} with N_d was small compared with N_a because L_p is much smaller than L_n, resulting in less changes in the collection efficiency of EHPs.

Figure 6b shows that V_{OC} initially increased rapidly but subsequently decreased slowly as N_a increased, as depicted in the 3D surface wireframe perpendicular to the N_d direction. The dependence of V_{OC} on N_d exhibits a similar trend. The maximum V_{OC} of 2.66 V is obtained by combining $N_a = 3.16 \times 10^{18}$ cm^{-3} and $N_d = 7.94 \times 10^{17}$ cm^{-3}. The bottom-projected contour indicates that the optimal values of V_{OC} are achieved at higher doping concentrations, which

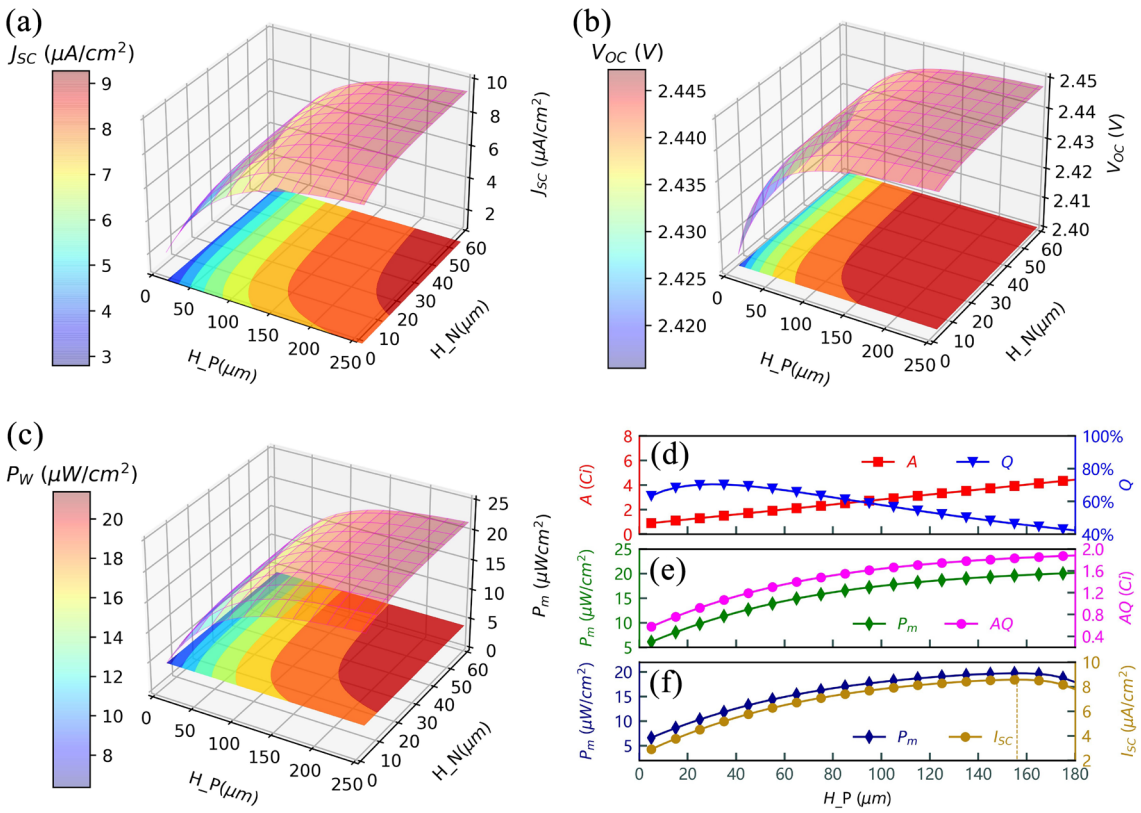

Fig. 5 (Color online) Effects of *H*_P and *H*_N on **a** J_{SC}, **b** V_{OC}, and **c** P_m with varying *H*_source; dependences of **d** *A*, *Q*, **e** P_m, and $A{\cdot}Q$ on *H*_P with *H*_N fixed at 24 μm; **f** dependence of P_m on *H*_P with *H*_source = 200 μm. N_a and N_d are both set to 1×10^{14} cm^{-3}, $t = 0.8$ μm, and $d = 1.2$ μm

is attributed to the reduction in the leakage current [J_0] owing to the higher doping concentration, as demonstrated in Fig. S3 in Supplementary Material.

Although J_{SC} and V_{OC} exhibit opposite dependencies on doping concentration, P_m varies in the same way as J_{SC} because the variation range of V_{OC} with doping concentration is small, of 2.44–2.66 V with a relative increase of 8.98%. The optimal doping concentration combination is $N_a = 1\times10^{14}$ cm^{-3} and $N_d = 1\times10^{14}$ cm^{-3}, yielding the maximum output power density of 19.74 μW/cm^2.

As shown in Fig. 6d, low doping increased *Q* from 13.48 to 45.65% owing to the widened depletion region and diffusion length, leading to longer ECR length [*H*_ECR] and improved EHP collection, and resulting in a higher power density. *H*_ECR and P_m follow a similar trend as *Q*, confirming that low doping enhances the power density by increasing *H*_ECR for EHP collection. However, at the highest doping concentration, *H*_ECR and P_m are minimum, of 53 μm and 6.37 μW/cm^2, respectively, which are only slightly better than the power of 5.80 μW/cm^2 with the *H*_source of 53 μm. P_m only marginally improves even with a nearly four-fold increase in the source activity [*A*], indicating the critical role of *H*_ECR in the design of the 3D battery and that *H*_source should not exceed *H*_ECR.

Additionally, *FF* ranges from 94.18 to 94.57%, with a tiny relative increase of 0.42%, while *A*, η_s, and $(1-r)$ remain constant at 4.04 Ci, 61.53%, and 48.77%, respectively, resulting in constant P_{in} of 129.16 μW/cm^2. Therefore, *Q* is a significant factor affecting the output power density, and a low doping concentration in the P- and N-regions is recommended to enhance it, hence maximizing the short current and output power density. Detailed calculations are provided in Supplementary Material S4.

3.1.4 Critical parameters of device structure

To achieve the best device performance, we comprehensively optimized the geometric dimensions (optimization procedure #1), doping concentration (optimization procedure #2), and width of each doping layer (optimization procedure #3) of the semiconductor materials. The final optimized parameters for the battery are $N_a = N_d = 1\times10^{14}$ cm^{-3}, *H*_P = 156 μm, *H*_N = 28 μm, $t = 0.8$ μm, and $d = 1.2$ μm.

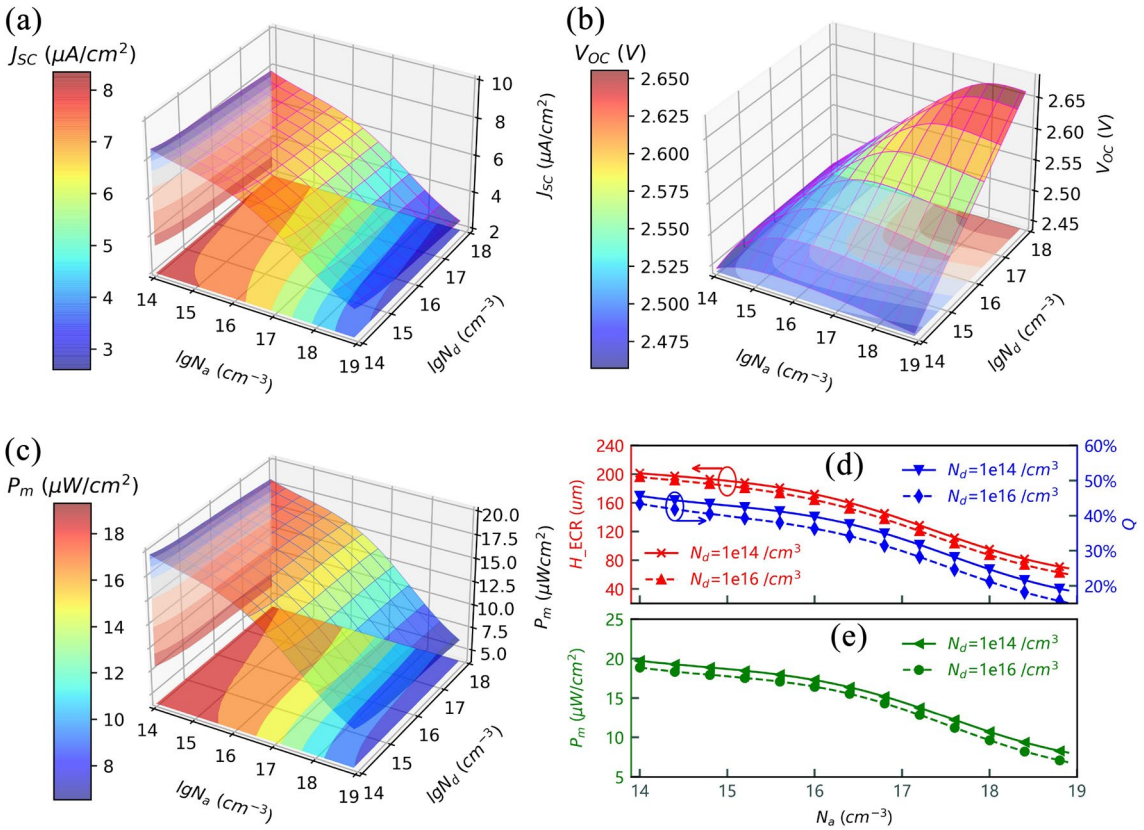

Fig. 6 (Color online) Influence of N_a and N_d on **a** J_{SC}, **b** V_{OC}, and **c** P_m; effect of N_a on **d** H_ECR, Q, and **e** P_m. H_P = 156 μm, H_N = 28 μm, t = 0.8 μm, and d = 1.2 μm

In Optimization procedure #1, A, η_s, and $(1-r)$ exhibited significant relative increases, while the relative increases in Q, V_{OC}, and FF were negligible, as shown in Fig. 7a. Therefore, the key factor affecting the output power is the coupling of A, η_s, and $(1-r)$, and a tradeoff between them is required to maximize the power density, as depicted by their optimal parameters corresponding to the maximum output power.

In Optimization procedure #2, A was identified as the dominant factor affecting the output power, with the significant relative increase of 1204.00%, and Q was a secondary factor with the relative increase of 164.92%, as depicted in Fig. 7b. Increasing H_P and H_N can enhance the source activity [A] and ECR length. However, increasing H_P and H_N beyond the ECR leads to Q, as EHPs outside the ECR become difficult to collect. The tradeoff between A increasing and Q dropping results in saturation of the output power.

In Optimization procedure #3, we found that Q is the key factor affecting the output power; whereas, the other factors have negligible relative increases, as shown in Fig. 7c. To optimize the output power density, low doping concentrations should be used in both P- and N-regions. This enables larger diffusion lengths and wider ECRs, resulting in a higher collection efficiency of EHPs, particularly through an extended H_ECR.

Among these parameters, the coupling of A, η_s, and $(1-r)$ has the greatest impact on the output performance, which is related to the activity, self-absorption, and backscattering of the radioactive source. The second most influential parameter is Q, which depends on the depletion region width and diffusion length controlled by the doping concentration, as well as the ECR length governed by H_P, H_N, and the doping concentration. To maximize the output power density, use of thinner sources and converters, lower doping concentrations, and larger H_P, of approximately twice the diffusion length, are recommended.

To validate the numerical model established in this study, we performed calculations on planar batteries with the same geometric dimensions and semiconductor parameters as those in references [24] and [16]; good agreement was apparent regarding the output power density, as shown in Table 3. It is worth noting that the power density of battery #1 was converted based on the 100% abundance of ^{63}Ni source, in contrast to the 20% abundance mentioned in reference [24]. The difference in the results between reference [16] and this study (#5 battery) is relatively large because

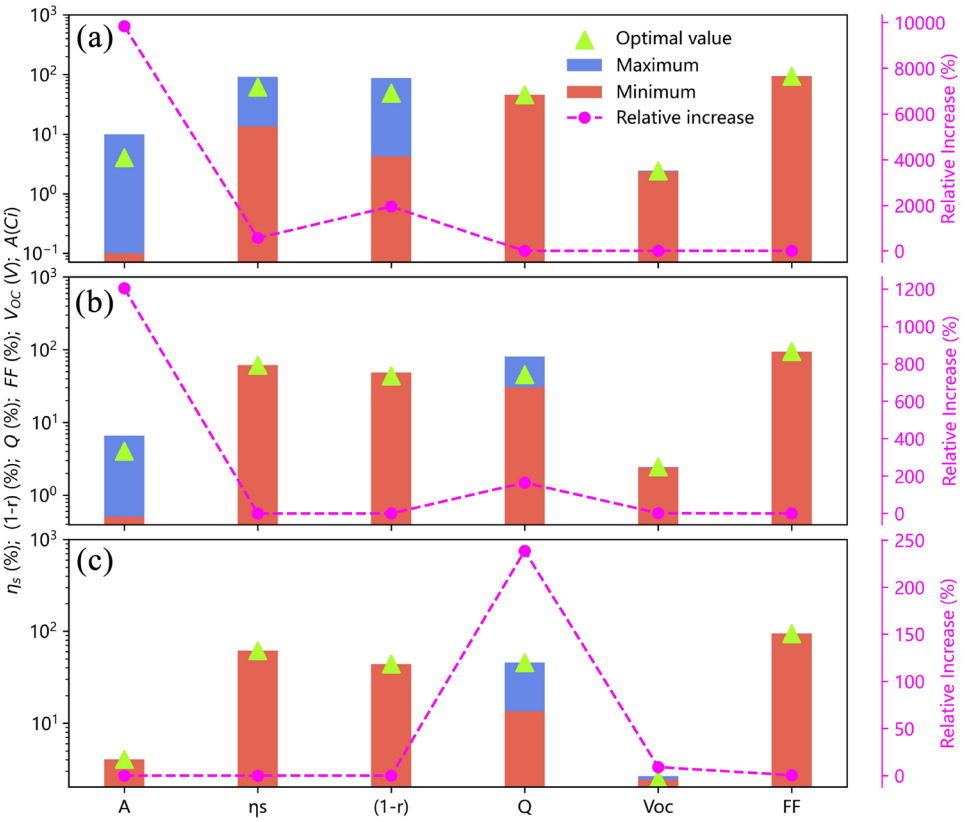

Fig. 7 (Color online) Optimal parameters and their relative increase considering different optimization procedures: **a** Optimizing t and d; **b** Optimizing H_P and H_N; **c** Optimizing N_a and N_d. Relative increase is calculated as the difference between the maximum and minimum values divided by the minimum value. The bars show the minimum values only, indicating that the maximum value is equal to the minimum

Table 3 Comparison between our battery model results and previous works; optimization suggestions for the batteries in references; comparative analysis between the P^+PNN^+ structure and the PN structure

Battery ID	Type	Source thickness (μm)	Converter thickness (μm)	Doping concentration (cm^{-3})	P_m (nW/cm^2)	Ref.
#1	2D-P^+PNN^+	1	P^+\P\N\N^+: 0.1\23.9\0.9\0.1	P^+\P\N\$N^+$: 10^{19}\$10^{13}$\$10^{16}$\$10^{19}$	269.1	[24]
#2	2D-P^+PNN^+	1			263.3	Our work for validating
#3	2D-P^+PNN^+	1	P^+\P\N\N^+: 0.1\4.9\19.9\0.1	P^+\P\N\$N^+$: 10^{19}\$10^{14}$\$3.98\times10^{14}$\$10^{19}$	296.5	Our work for optimizing
#4	PN	2	P\N: 8\15	P\N: 4.7×10^{13}\$3\times10^{16}$	360	[16]
#5	PN	2			342	Our work for validating
#6	PN	2	0.1\22.9	4.7×10^{13}\$3\times10^{16}$	378	Our work for optimizing
#7	2D-P^+PNN^+	2	P^+\P\N\N^+: 0.1\4.9\19.9\0.1	P^+\P\N\$N^+$: 10^{19}\$10^{14}$\$3.98\times10^{14}$\$10^{19}$	394	Our work for comparing
#8	2D- PN	2	P\N: 5\20	P\N: 10^{14}\$3.98\times10^{14}$	358	
#9	3D-P^+PNN^+	0.8	P^+\P\N\N^+: 10\156\28\6	P^+\P\N\$N^+$: 10^{19}\$10^{14}$\$10^{14}$\$10^{18}$	19.74 μW/cm^2	
#10	3D-PN	0.8	P\N: 166\34	P\N:10^{14}\$10^{14}$	14.22 μW/cm^2	

the previous work did not consider the energy loss caused by the collection efficiency Q, leading to an overestimation of P_m. Using our method, we can further provide suggestions for optimizing the batteries in references [24] and [16] by adjusting N_a, N_d, H_P and H_N. For reference [24], setting H_P, H_N, N_a, and N_d to 4.9 μm, 19.9 μm, 1×10^{14} cm^{-3}, and 3.98×10^{14} cm^{-3}, respectively, the maximum output power can be increased to 296.5 nW/cm^2, representing a 12.6%

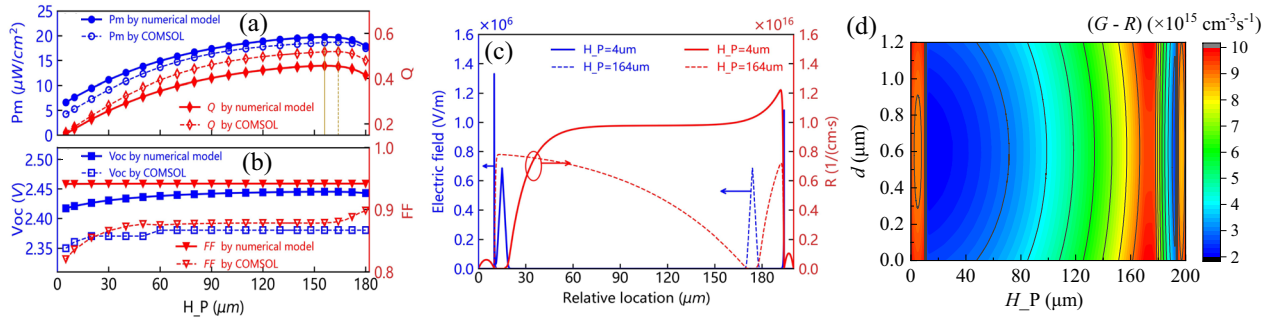

Fig. 8 (Color online) Discrepancies between the ideal and practical performances simulated by COMSOL: **a** Dependences of P_m, Q, **b** V_{OC}, and FF on H_P; **c** Distribution of electric field and carrier recombination rate; **d** Dependences of (G-R) distribution on H_P and d. (G–R) represents the difference between the generation rate and the recombination rate of EHPs

improvement as depicted by battery #3. For reference [16], by combining $H\_P = 0.1$ μm, N_a and N_d at 4.7×10^{13} cm^{-3} and 3×10^{16} cm^{-3}, respectively, the output power can be increased to 378 nW/cm^2, with a 10.5% improvement as depicted by battery #6.

Finally, we conducted a comparative analysis of the P$^+$PNN$^+$ and PN structures, assessing their respective output power densities in the 2D (#7 and #8) and 3D (#9 and #10) batteries. To achieve this, we substituted the P$^+$ and N$^+$ layers in the P$^+$PNN$^+$ structure with P and N layers of the same size to obtain the PN structure, as shown in Table 3. Our results indicate that the P$^+$PNN$^+$ structure outperforms the PN structure, with a 10% increase in P_m in the 2D configuration and a 39% increase in the 3D configuration. These findings highlight the superior performance of the P$^+$PNN$^+$ structure, particularly in 3D configurations.

In this study, the diffusion lengths were calculated through commonly used equations [17, 42], and the minority carrier lifetimes (τ_n and τ_p) adopted in these calculations (shown in Supplementary Material S4) fall within the range of experimental values (τ_n of 0.9–10 μs and τ_p of 0.05–2.1 μs) [47–50]. Moreover, experimental diffusion lengths for SiC were reported to be 30–100 μm [49, 51], which provides further validation for the calculated electron and hole diffusion lengths presented in this article.

3.2 Performance simulation using COMSOL Multiphysics

The largest discrepancies between the ideal and practical performances of betavoltaic nuclear battery are the collection efficiency Q and V_{OC} FF/ε [10]. To better understand the discrepancies between the ideal and practical performance of betavoltaic nuclear batteries, it is necessary to conduct a detailed analysis of the specific differences caused by Q, V_{OC}, and FF, as well as their underlying reasons. COMSOL Multiphysics was employed to simulate the practical performance of betavoltaic batteries. Most SiC material properties were imported from the COMSOL library; some properties that were not available in the library, such as minority carrier mobility and minority carrier lifetime, were manually added based on the literature [17].

In the simulation process, a single converter was modeled with dimensions of 1 μm × 1.2 μm × 200 μm. A user-controlled mesh of four different sizes (#a, #b, #c, and #d) was defined to improve both the accuracy and computation time, with maximum element sizes of 50, 100, 200, and 500 nm. The minimum element sizes were set to 1/10 of the corresponding maximum element sizes. Although the use of finer mesh sizes resulted in slightly larger P_m values, the differences are negligible. Specifically, P_m values obtained from mesh #a are only 0.064%, 0.121%, and 0.149% higher than those obtained from meshes #b, #c, and #d, respectively. Based on these results, the #d mesh was chosen for computation, with boundary elements set at the maximum element size of 0.1 and minimum element size of 0.02. The maximum element growth rate was set to 1.1 with the curvature factor of 0.25, and the resolution of the narrow regions was specified as 1.

Figure 8a displays the relationship between P_m and H_P obtained through numerical modeling and COMSOL simulations. The variations in P_m with H_P from these two methods are in excellent agreement, reaching their maximum values at H_P of 156 and 164 μm, respectively, with values of 19.74 and 18.69 μW/cm^2, differing by only 5.62%. However, there were some differences in P_m at lower values of H_P, which increased as H_P decreased. These differences arise from Q, V_{OC}, and FF, as shown in Fig. 8a, b, respectively. The numerical model relies on empirical formulas (4) and (12) for Q and V_{OC}, resulting in a lower Q and higher V_{OC} than the COMSOL simulation, which calculates Q by subtracting the Shockley-Reed-Hall recombination rate from the EHP generation rate (shown in Fig. 8d) and extracting V_{OC} by finding the voltage value when the current is nearly zero. In addition, the numerical model produces a higher FF with little variation, while the COMSOL simulation calculates

FF by dividing P_m by V_{OC} and J_{SC}, which are sensitive to the distribution of V_{OC}.

In addition, P_m initially increases and then decreases with increasing *H*_P, reaching a maximum value at *H*_P of approximately $2L_n$. This can be explained by the suppression of carrier recombination owing to the electric field distribution. The electric field distribution intensity and range at *H*_P = 164 μm are much greater than those at *H*_P = 4 μm, resulting in a considerably lower carrier recombination rate, leading to a larger *Q* and hence a larger P_m, shown in Fig. 8c. This indicates that the internal mechanism affecting the power increase is the electric field distribution, which governs the carrier transport and collection characteristics.

The results demonstrate that the proposed battery has a significantly improved output performance compared with conventional planar batteries reported in previous studies [13–16, 19, 23, 24], with a maximum output power density approximately 50 times higher. If multiple batteries are stacked to a total thickness of around 10 mm, the proposed battery would provide an output power of approximately 1 mW, which can satisfy the power requirements of MEMS with dimensions less than 10 mm and power consumption of 1–100 μW. We provide further recommendations for designing 3D-groove betavoltaic nuclear batteries regarding 3D etching techniques on SiC, as shown in Table S2 of the Supplementary Material.

4 Conclusion

In summary, this paper presents a novel ^{63}Ni-SiC-based P^+PNN^+ 3D structure with a multi-groove design that eliminates the need for preparing a PN junction on the inner surface of the microstructure and improves the performance of betavoltaic nuclear batteries. The fully coupled model developed in this study considers various factors, such as β-particle generation, self-absorption, backscattering, energy deposition, as well as radiation-induced carrier generation and drift–diffusion, and thus provides a valuable tool for efficient design and development of betavoltaic nuclear batteries with complex 3D structures. The epitaxially grown graded P/N layer significantly enhances *H*_ECR, promoting radioisotope source activity and carrier collection efficiency, producing the maximum output power density of 19.74 μW/cm^2, with relatively thin radioisotope sources and converters (t = 0.8 μm and d = 1.2 μm), lightly doped P- and N-regions ($N_a = N_d = 10^{14}$ cm^{-3}), and longer P-region widths (*H*_P = 156 μm). The analysis of carrier transport and collection characteristics using the COMSOL Multiphysics code provides insights into the internal mechanism of the power increase and clarifies the discrepancies between the ideal and simulated performances of betavoltaic nuclear batteries. However, the diffusion length is susceptible to process variations and a short diffusion length may reduce the advantages of the proposed P^+PNN^+ 3D structure. In conclusion, the proposed 3D structure with a multi-groove design combined with a fully coupled model and optimization methods presents a promising approach for designing and optimizing high-performance betavoltaic nuclear batteries. It is worth noting that the importance of *H*_ECR cannot be overstated by increasing the output power, as it directly affects both radioisotope source loading and charge collection efficiency. Furthermore, the 3D structure proposed herein is expected to be well-suited for narrow-bandgap semiconductor materials with ultralong diffusion lengths.

See the supplementary material for details of our calculation procedure and recommendations on the device design of betavoltaic nuclear batteries considering three-dimensional etching techniques on SiC.

Supplementary Information The online version contains supplementary material available at https://doi.org/10.1007/s41365-023-01331-y.

Author contributions All authors contributed to the study conception and design. Material preparation, data collection and analysis were performed by Hou-Jun He, Yun-Cheng Han, Xiao-Yu Wang, Yu-Min Liu, Jia-Chen Zhang, Lei Ren and Ming-Jie Zheng. The first draft of the manuscript was written by Hou-Jun He and all authors commented on previous versions of the manuscript. All authors read and approved the final manuscript.

Data availability The data that support the findings of this study are openly available in Science Data Bank at https://www.doi.org/10.57760/sciencedb.j00186.00275 and https://cstr.cn/31253.11.sciencedb.j00186.00275.

Declarations

Conflict of interest The authors declare that they have no competing interests.

References

1. W.Z. Yuan, D.Y. Qiao, *Micro-Electro-Mechanical System (MEMS) Manufacturing Technology* (Science Press, Beijing, 2014)
2. C. Thomas, S. Portnoff, M.G. Spencer, High efficiency 4H-SiC betavoltaic power sources using tritium radioisotopes. Appl. Phys. Lett. **108**, 013505 (2016). https://doi.org/10.1063/1.4939203
3. S.G. Kim, S. Priya, I. Kanno, Piezoelectric MEMS for energy harvesting. MRS Bull. **37**, 1039–1050 (2012). https://doi.org/10.1557/mrs.2012.275
4. O.M. Barham, Comparing nuclear and chemical power sources for MEMS/NEMS applications. in *ASME 2021 International Design Engineering technical Conferences and Computers and Information in Engineering Conference. Volume 11: 15th International Conference on Micro- and Nanosystems (MNS)*, (2021). https://doi.org/10.1115/detc2021-68110
5. A.V. Sachenko, A.I. Shkrebtii, R.M. Korkishko et al., Efficiency analysis of betavoltaic elements. Solid State Electron. **111**, 147–152 (2015). https://doi.org/10.1016/j.sse.2015.05.042
6. H.Y. Chen, L. Jiang, X.Y. Chen, Design optimization of GaAs betavoltaic batteries. J. Phys. D Appl. Phys. **44**, 215303 (2011). https://doi.org/10.1088/0022-3727/44/21/215303

7. M. Lu, G.-G. Zhang, K. Fu et al., Gallium nitride Schottky betavoltaic nuclear batteries. Energ. Convers. Manage. **52**, 1955–1958 (2011). https://doi.org/10.1016/j.enconman.2010.10.048
8. T.R. Alam, M.A. Pierson, M.A. Prelas, Beta particle transport and its impact on betavoltaic battery modeling. Appl. Radiat. Isotopes. **130**, 80–89 (2017). https://doi.org/10.1016/j.apradiso.2017.09.009
9. S.I. Maximenko, J.E. Moore, C.A. Affouda et al., Optimal semiconductors for 3H and 63Ni betavoltaics. Sci. Rep. **9**, 10892 (2019). https://doi.org/10.1038/s41598-019-47371-6
10. C. Zhao, F. Liao, K. Liu et al., Breaking the myth: wide-bandgap semiconductors not always the best for betavoltaic batteries. Appl. Phys. Lett. **119**, 153904 (2021). https://doi.org/10.1063/5.0068269
11. C. Zhao, A. Liu, S. Bai et al., Understanding efficiency differences of betavoltaic batteries measured by electron gun mimicked source and radioactive β source. Appl. Phys. Lett. **117**, 193901 (2020). https://doi.org/10.1063/5.0028450
12. A. Belghachi, K. Bozkurt, O. Ozdemir et al., Enhancement of Ni-63 planar source efficiency for betavoltaic batteries. J. Phys. D Appl. Phys. **53**, 445501 (2020). https://doi.org/10.1088/1361-6463/ab9977
13. X.B. Tang, D. Ding, Y.P. Liu et al., Optimization design and analysis of Si–63Ni betavoltaic battery. Sci. China Tech. Sci. **55**, 990–996 (2012). https://doi.org/10.1007/s11431-012-4752-6
14. F. Bouzid, S. Dehimi, M. Hadjab et al., Performance prediction of AlGaAs/GaAs betavoltaic cells irradiated by nickel-63 radioisotope. Physica B **607**, 412850 (2021). https://doi.org/10.1016/j.physb.2021.412850
15. R.Z. Zheng, J.B. Lu, Y. Wang et al., Understanding efficiency improvements of betavoltaic batteries based on 4H–SiC, GaN, and diamond. Appl. Phys. Lett. **121**, 103902 (2022). https://doi.org/10.1063/5.0102995
16. Y.M. Liu, J.B. Lu, X.Y. Li et al., A 4H–SiC betavoltaic battery based on a 63Ni source. Nucl. Sci. Tech. **29**, 168 (2018). https://doi.org/10.1007/s41365-018-0494-x
17. L. Zhang, H.L. Cheng, X.C. Hu et al., Model and optimal design of 147Pm SiC-based betavoltaic cell. Superlattice. Microst. **123**, 60–70 (2018). https://doi.org/10.1016/j.spmi.2018.01.007
18. G.Q. Wang, H. Li, Y. Lei et al., Demonstration of Pm-147 GaN betavoltaic cells. Nucl. Sci. Tech. **25**, 020403 (2014). https://doi.org/10.13538/j.1001-8042/nst.25.020403
19. C.E. Munson, Q. Gaimard, K. Merghem et al., Modeling, design, fabrication and experimentation of a GaN-based, 63Ni betavoltaic battery. J. Phys. D Appl. Phys. **51**, 035101 (2018). https://doi.org/10.1088/1361-6463/aa9e41
20. A. Krasnov, S. Legotin, K. Kuzmina et al., A nuclear battery based on silicon pin structures with electroplating 63Ni layer. Nucl. Eng. Technol. **51**, 1978–1982 (2019). https://doi.org/10.1016/j.net.2019.06.003
21. Y. Liu, R. Hu, Y. Yang et al., Investigation on a radiation tolerant betavoltaic battery based on Schottky barrier diode. Appl. Radiat. Isotopes. **70**, 438–441 (2012). https://doi.org/10.1016/j.apradiso.2011.10.013
22. H. Guo, Y. Shi, Y. Zhang et al., Fabrication of SiC p–i–n betavoltaic cell with 63Ni irradiation source. in *2011 IEEE International Conference of Electron Devices and Solid-State Circuits*. (2011), pp. 1–2. https://doi.org/10.1109/EDSSC.2011.6117636
23. S. Yao, Z. Song, X. Wang et al., Design and simulation of betavoltaic battery using large-grain polysilicon. Appl. Radiat. Isotopes. **70**, 2388–2394 (2012). https://doi.org/10.1016/j.apradiso.2012.06.009
24. G. Gui, K. Zhang, J.P. Blanchard et al., Prediction of 4H-SiC betavoltaic microbattery characteristics based on practical Ni-63 sources. Appl. Radiat. Isotopes. **107**, 272–277 (2016). https://doi.org/10.1016/j.apradiso.2015.11.001
25. Z.J. Cheng, X.Y. Chen, H.S. San et al., A high open-circuit voltage gallium nitride betavoltaic microbattery. J. Micromech. Microeng. **22**, 074011 (2012). https://doi.org/10.1088/0960-1317/22/7/074011
26. W. Sun, N.P. Kherani, K.D. Hirschman et al., A three-dimensional porous silicon p–n diode for betavoltaics and photovoltaics. Adv. Mater. **17**, 1230–1233 (2005). https://doi.org/10.1002/adma.200401723
27. A.A. Krasnov, V.V. Starkov, S.A. Legotin et al., Development of betavoltaic cell technology production based on microchannel silicon and its electrical parameters evaluation. Appl. Radiat. Isotopes. **121**, 71–75 (2017). https://doi.org/10.1016/j.apradiso.2016.12.019
28. J.W. Murphy, C.D. Frye, R.A. Henderson et al., Demonstration of a three-dimensionally structured betavoltaic. J. Electron. Mater. **50**, 1380–1385 (2021). https://doi.org/10.1007/s11664-020-08611-y
29. Z. Ding, T.X. Jiang, R.R. Zheng et al., Quantitative modeling, optimization, and verification of 63Ni-powered betavoltaic cells based on three-dimensional ZnO nanorod arrays. Nucl. Sci. Tech. **33**, 144 (2022). https://doi.org/10.1007/s41365-022-01127-6
30. A.A. Krasnov, S.A. Legotin, Advances in the development of betavoltaic power sources (a review). Instrum. Exp. Tech+. **63**, 437–452 (2020). https://doi.org/10.1134/s0020441220040156
31. Y.J. Yoon, J.S. Lee, I.M. Kang et al., Design and optimization of GaN-based betavoltaic cell for enhanced output power density. Int. J. Energ. Res. **45**, 799–806 (2021). https://doi.org/10.1002/er.5909
32. F. Rahmani, H. Khosravinia, Optimization of silicon parameters as a betavoltaic battery: comparison of Si pn and Ni/Si Schottky barrier. Radiat. Phys. Chem. **125**, 205–212 (2016). https://doi.org/10.1016/j.radphyschem.2016.04.012
33. W. Li, K. Nomoto, Z. Hu et al., Field-plated Ga_2O_3 Trench Schottky barrier diodes with a BV2/Ron, sp of up to 0.95 GW/cm^2. IEEE Electr. Dev. L. **41**, 107–110 (2019). https://doi.org/10.1109/LED.2019.2953559
34. J. Yota, H. Shen, R. Ramanathan, Characterization of atomic layer deposition HfO2, Al2O3, and plasma-enhanced chemical vapor deposition Si3N4 as metal-insulator-metal capacitor dielectric for GaAs HBT technology. J. Vac. Sci. Technol. A **31**, 01A134 (2013). https://doi.org/10.1116/1.4769207
35. N. Alimardani, J.F. Conley, Enhancing metal-insulator-insulator-metal tunnel diodes via defect enhanced direct tunneling. Appl. Phys. Lett. **105**, 082902 (2014). https://doi.org/10.1063/1.4893735
36. R. Singh, T.R. Lenka, D.K. Panda et al., The dawn of Ga_2O_3 HEMTs for high power electronics: a review. Mat. Sci. Semicon. Proc. **119**, 105216 (2020). https://doi.org/10.1016/j.mssp.2020.105216
37. D.Y. Qiao, W.Z. Yuan, P. Gao et al., Demonstration of a 4H SiC betavoltaic nuclear battery based on Schottky barrier diode. Chin. Phys. Lett. **25**, 3798 (2008). https://doi.org/10.1088/0256-307X/25/10/076
38. X.Y. Li, Y. Ren, X.J. Chen et al., 63Ni schottky barrier nuclear battery of 4H-SiC. J. Radioanal. Nucl. Ch. **287**, 173–176 (2011). https://doi.org/10.1007/s10967-010-0746-7
39. K. Vanthanh, Y.C. Ma, J.H. Si et al., Fabrication of micro-grooves in silicon carbide using femtosecond laser irradiation and acid etching. Chin. Phys. Lett. **31**, 037901 (2014). https://doi.org/10.1088/0256-307X/31/3/037901
40. B.J. Baliga, *Fundamentals of Power Semiconductor Devices* (Springer Science & Business Media, 2010)
41. A.A. Svintsov, A.A. Krasnov, M.A. Polikarpov et al., Betavoltaic battery performance: comparison of modeling and experiment.

Appl. Radiat. Isotopes. **137**, 184–189 (2018). https://doi.org/10.1016/j.apradiso.2018.04.010
42. C. Zhao, L. Lei, F.Y. Liao et al., Efficiency prediction of planar betavoltaic batteries basing on precise modeling of semiconductor units. Appl. Phys. Lett. **117**, 263901 (2020). https://doi.org/10.1063/5.0033052
43. S. Mohamadian, S. Feghhi, H. Afarideh, Analyze and simulation of a typical MEMS RPG using MCNP code. Int. Conf. Nucl. Eng. **48140**, 883–886 (2008). https://doi.org/10.1115/ICONE16-48766
44. X. Li, N.P. Hylton, V. Giannini et al., Multi-dimensional modeling of solar cells with electromagnetic and carrier transport calculations. Prog. Photovolt. **21**, 109–120 (2013). https://doi.org/10.1002/pip.2159
45. Q.J. Meng, H.B. Liu, Q.H. Meng, *Physics of Semiconductor Devices* (Science Press, Beijing, 2005)
46. M. Grundmann, Diodes. in M. Grundmann (Ed.) *The Physics of Semiconductors: An Introduction Including Nanophysics and Applications*. (Springer International Publishing, Cham, 2016), pp. 583–667. https://doi.org/10.1007/978-3-319-23880-7_21
47. T. Okuda, T. Miyazawa, H. Tsuchida et al., Carrier lifetimes in lightly-doped p-Type 4H-SiC epitaxial layers enhanced by post-growth processes and surface passivation. J. Electron. Mater. **46**, 6411–6417 (2017). https://doi.org/10.1007/s11664-017-5677-4
48. J. Zhang, L. Storasta, J.P. Bergman et al., Electrically active defects inn-type 4H–silicon carbide grown in a vertical hot-wall reactor. J. Appl. Phys. **93**, 4708–4714 (2003). https://doi.org/10.1063/1.1543240
49. B.J. Baliga, *The Igbt Device: Physics, Design and Applications of the Insulated Gate Bipolar Transistor* (Elsevier, Waltham, 2015)
50. O. Kordina, J.P. Bergman, C. Hallin et al., The minority carrier lifetime of n-type 4H- and 6H-SiC epitaxial layers. Appl. Phys. Lett. **69**, 679–681 (1996). https://doi.org/10.1063/1.117804
51. P. Ščajev, K. Jarašiūnas, Temperature- and excitation-dependent carrier diffusivity and recombination rate in 4H–SiC. J. Phys. D Appl. Phys. **46**, 265304 (2013). https://doi.org/10.1088/0022-3727/46/26/265304

Authors and Affiliations

Hou-Jun He[1,2,3] · Yun-Cheng Han[1] · Xiao-Yu Wang[1,4] · Yu-Min Liu[3] · Jia-Chen Zhang[1,2] · Lei Ren[1,2] · Ming-Jie Zheng[1]

✉ Xiao-Yu Wang
wangxy@inest.cas.cn

✉ Ming-Jie Zheng
mingjie.zheng@inest.cas.cn

[1] Hefei Institutes of Physical Science, Chinese Academy of Sciences, Hefei 230031, China

[2] University of Science and Technology of China, Hefei 230026, China

[3] School of Nuclear Science and Engineering, East China University of Technology, Nanchang 330013, China

[4] School of Nuclear Technology and Chemistry and Biology, Hubei University of Science and Technology, Xianning 437100, China